

Controllable Spin Current in van der Waals Ferromagnet Fe_3GeTe_2

Jiaqi Zhou* and Jean-Christophe Charlier†

*Institute of Condensed Matter and Nanosciences (IMCN),
Université catholique de Louvain, B-1348, Louvain-la-Neuve, Belgium*

(Dated: September 28, 2021)

The control of spin current is pivotal for spintronic applications, especially for spin-orbit torque devices. Spin Hall effect (SHE) is a prevalent method to generate spin current. However, it is difficult to manipulate its spin polarization in nonmagnet. Recently, the discovery of spin current in ferromagnet offers opportunity to realize the manipulation. In the present work, the spin current in van der Waals ferromagnet Fe_3GeTe_2 (FGT) with varying magnetization is theoretically investigated. It has been observed that the spin current in FGT presents a nonlinear behavior with respect to magnetization. The in-plane and out-of-plane spin polarizations emerge simultaneously, and the bilayer FGT can even exhibit arbitrary polarization thanks to the reduced symmetry. More intriguingly, the correlation between anomalous Hall effect (AHE) and spin anomalous Hall effect (SAHE) has been interpreted from the aspect of Berry curvature and spin. This work illustrates that the interplay of magnetism and symmetry can effectively control the magnitude and polarization of the spin current, providing a practical method to realize exotic spin-orbit torques.

Introduction.—The spin-orbit-coupling (SOC) effects are the frontier of spintronics and attract widespread interests. Versatile SOC effects stimulate fascinating phenomena, and improve the performances of magnetic random access memory (MRAM) [1, 2]. For instance, the perpendicular magnetic anisotropy (PMA) greatly increases the storage density of MRAM [3], and the spin-orbit torque (SOT) can realize ultrafast switching as well as low-power writing operation [4]. The last decade has witnessed the endeavor of researchers to realize the SOT switching [5]. The conventional SOT device consists of a ferromagnet/heavy metal bilayer structure, and the spin current in heavy metal is employed to induce SOT and switch the magnetization of ferromagnet [6, 7]. Spin current can be generated by the spin Hall effect (SHE) [8]. However, due to the constraint on SHE imposed by crystal symmetry, the torque of perpendicular-flowing spin current is limited to be in-plane [6]. Thus, the switching of perpendicular magnetization requires an external magnetic field, which hinders the device minimization. To solve this difficulty, various methods have been proposed, such as the assistance of spin-transfer torque [9], the asymmetric structural design [10], as well as using low-symmetry crystals as torque sources [11–13]. More intriguingly, recent efforts have been expanded to explore the spin current in ferromagnet [14–17]. Superior to heavy metal, the magnetization in ferromagnet can break the constraint of symmetry, thus enabling diverse polarizations of spin current.

The spin current in ferromagnet can be attributed to the anomalous Hall effect (AHE) [18]. When the anomalous Hall current, i.e. spin-polarized current, occurs in ferromagnet, it is naturally accompanied by a pure spin current. This phenomenon is called the spin anomalous Hall effect (SAHE), where the spin polarization is collinear with magnetization [15]. Several experimental

and theoretical works have reported the spin current in ferromagnets. Generally, experimental works claim that the spin currents in ferromagnets completely originate from SAHE [15, 19, 20]. However, contradictory results appeared regarding whether the spin current is dependent on the magnetization of ferromagnet [15–17, 19–22]. Meanwhile, theoretical works also present different interpretations. It has been stated that the spin component transverse to the magnetization rapidly precesses and dephases in a ferromagnet, suggesting that the spin current only has the spin along the magnetization, and its origin is SAHE exclusively [14]. However, recent first-principles simulations demonstrate that the spin current in $3d$ ferromagnet is composed of two contributions, SAHE and SHE. The former is dependent on the magnetization while the latter is not. Moreover, the spin current with spin component transverse to the magnetization is protected from dephasing [23, 24]. Recently, the magnetization-dependent SHE is also reported in $3d$ ferromagnet [25]. In fact, the debate is focusing on the different definitions of SAHE and SHE. Indeed, although the previous theoretical works have already provided intuitive understandings of the spin current in ferromagnet, rigorous derivations of SAHE based on the linear response theory is still missing. Besides, even if current studies are limited to conventional $3d$ ferromagnet, the development of van der Waals (vdW) material provides two-dimensional (2D) ferromagnet [26, 27] as an ideal platform to investigate spin current. The representative material is the metallic Fe_3GeTe_2 (FGT), which can exhibit gate-tunable room-temperature ferromagnetism [28, 29]. Different from other cubic ferromagnets, FGT is a uniaxial crystal with low symmetry. More interestingly, changing the thickness can modify the phase of FGT few-layer, giving a broad space to investigate diverse spin current tensors.

In this Letter, the spin current in Fe_3GeTe_2 ferromagnet has been systematically investigated using *ab initio* calculations. The monolayer and bilayer FGT can exhibit nonlinear spin current with respect to magne-

* jiaqi.zhou@uclouvain.be

† jean-christophe.charlier@uclouvain.be

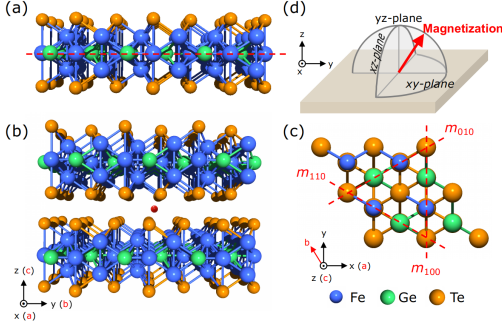


FIG. 1. (a) Atomic model of monolayer FGT with a mirror symmetry (the red dashed line). (b) Atomic model of bilayer FGT with an inversion center (the red point). (c) Top view of bilayer FGT including mirror symmetries. Fe, Ge, and Te are represented by blue, green, and orange balls, respectively. (d) Illustration of the magnetization evolution in different planes.

tization, making its magnitude controllable. More intriguingly, both the magnetization and the low-symmetry structure of FGT can break the constraint on spin current tensors, enabling the simultaneous occurrence of in-plane and out-of-plane spin polarizations. Using the Kubo formula, the origin of spin current is classified according to the spin, and the correlation between AHE and SAHE is clarified. This work demonstrates that the interplay of magnetism and symmetry can create unconventional spin current, as well as interprets the origin of spin current in ferromagnet.

Models and methods.—The shape of linear response tensors of an electric field is restricted by the symmetry of crystal [30–33]. Consequently, crystals in different phases would exhibit various Hall currents [34]. FGT is a uniaxial crystal in the hexagonal structure. Even if both exhibit three mirrors orthogonal to the xy -plane as shown in Fig. 1(c), the monolayer FGT crystallizes in $P\bar{6}m2$ phase with a mirror \mathcal{M} normal to z -direction [see Fig. 1(a)], while the bilayer FGT is in $P\bar{3}m1$ phase with the spatial inversion \mathcal{P} [see Fig. 1(b)]. The structural discrepancy creates opportunity to explore various Hall currents in these two types of FGT. The intrinsic anomalous Hall conductivity (AHC) and spin Hall conductivity (SHC) have been investigated using *ab initio* calculations, as implemented in QUANTUM ESPRESSO [35] and WANNIER90 [36], see details in Supplemental Material [37].

Definitions of Hall conductivities.—The present work focuses on the current along x -axis when the electric field is applied along y -axis. The spin polarization γ is projected onto the x , y , or z -axis.

In the 2D system, the anomalous Hall conductivity can be evaluated by Kubo formula as [38, 39]

$$\sigma_{\text{AH}} = -\frac{e^2}{\hbar} \int_{\text{BZ}} \frac{d^2k}{(2\pi)^2} \Omega(\mathbf{k}), \quad (1)$$

where BZ denotes the first Brillouin zone, $\Omega(\mathbf{k})$ is the

Berry curvature, as

$$\Omega(\mathbf{k}) = \sum_n f_{n\mathbf{k}} \Omega_n(\mathbf{k}), \quad (2)$$

$$\Omega_n(\mathbf{k}) = \hbar^2 \sum_{m \neq n} \frac{-2 \text{Im}[\langle n\mathbf{k} | \hat{v}_x | m\mathbf{k} \rangle \langle m\mathbf{k} | \hat{v}_y | n\mathbf{k} \rangle]}{(\epsilon_{n\mathbf{k}} - \epsilon_{m\mathbf{k}})^2}, \quad (3)$$

where $f_{n\mathbf{k}}$ is the Fermi-Dirac distribution function, n and m are the band indexes, $\epsilon_{n\mathbf{k}}$ and $\epsilon_{m\mathbf{k}}$ are the eigenvalues, \hat{v}_x and \hat{v}_y denote the velocity operators.

In analogy with that of nonmagnet [40, 41], the spin Hall conductivity of 2D ferromagnet is given as

$$\sigma_{\text{SH},\gamma} = -\frac{e^2}{\hbar} \int_{\text{BZ}} \frac{d^2k}{(2\pi)^2} \Omega_\gamma(\mathbf{k}), \quad (4)$$

where $\Omega_\gamma(\mathbf{k})$ is the spin Berry curvature, as

$$\Omega_\gamma(\mathbf{k}) = \sum_n f_{n\mathbf{k}} \Omega_{n,\gamma}(\mathbf{k}), \quad (5)$$

$$\Omega_{n,\gamma}(\mathbf{k}) = \hbar^2 \sum_{m \neq n} \frac{-2 \text{Im}[\langle n\mathbf{k} | \frac{1}{2} \{ \hat{\sigma}_\gamma, \hat{v}_x \} | m\mathbf{k} \rangle \langle m\mathbf{k} | \hat{v}_y | n\mathbf{k} \rangle]}{(\epsilon_{n\mathbf{k}} - \epsilon_{m\mathbf{k}})^2}, \quad (6)$$

where $\hat{\sigma}_\gamma$ is the spin operator, and $\frac{1}{2} \{ \hat{\sigma}_\gamma, \hat{v}_x \} = \frac{1}{2} (\hat{\sigma}_\gamma \hat{v}_x + \hat{v}_x \hat{\sigma}_\gamma)$.

Since both AHC and SHC occur in a ferromagnet, the correlation between them is worth investigation. Firstly we define a spin matrix \mathbf{S} whose dimension is the number of eigenstates, and element at the m th row and n th column is $\langle m\mathbf{k} | \hat{\sigma}_\gamma | n\mathbf{k} \rangle$. It can be seen that the n th diagonal element of \mathbf{S} is the spin of the n th eigenstate, called the *intra* band spin. Then, through inserting a projection operator $\sum_t |t\mathbf{k}\rangle \langle t\mathbf{k}| = 1$ into Eq. (6) and considering $t = n, m$, respectively, the diagonal elements of \mathbf{S} , i.e. $\langle n\mathbf{k} | \hat{\sigma}_\gamma | n\mathbf{k} \rangle$ and $\langle m\mathbf{k} | \hat{\sigma}_\gamma | m\mathbf{k} \rangle$, can be extracted. Since both $\langle n\mathbf{k} | \hat{\sigma}_\gamma | n\mathbf{k} \rangle$ and $\langle m\mathbf{k} | \hat{\sigma}_\gamma | m\mathbf{k} \rangle$ are real, this diagonal part can be denoted by $\bar{\Omega}_{n,\gamma}(\mathbf{k})$ as

$$\bar{\Omega}_{n,\gamma}(\mathbf{k}) = \hbar^2 \sum_{m \neq n} [\langle n\mathbf{k} | \hat{\sigma}_\gamma | n\mathbf{k} \rangle + \langle m\mathbf{k} | \hat{\sigma}_\gamma | m\mathbf{k} \rangle] \times \frac{-\text{Im}[\langle n\mathbf{k} | \hat{v}_x | m\mathbf{k} \rangle \langle m\mathbf{k} | \hat{v}_y | n\mathbf{k} \rangle]}{(\epsilon_{n\mathbf{k}} - \epsilon_{m\mathbf{k}})^2}. \quad (7)$$

As a result of the *intra* band spin, Eq. (7) is called the band-resolved *intra* spin Berry curvature. With this quantity and its summation over the occupied bands, the *intra* spin Hall conductivity is defined as

$$\bar{\Omega}_\gamma(\mathbf{k}) = \sum_n f_{n\mathbf{k}} \bar{\Omega}_{n,\gamma}(\mathbf{k}), \quad (8)$$

$$\sigma_{\text{SH},\gamma}^{\text{intra}} = -\frac{e^2}{\hbar} \int_{\text{BZ}} \frac{d^2k}{(2\pi)^2} \bar{\Omega}_\gamma(\mathbf{k}). \quad (9)$$

The correlation between AHC and *intra* SHC is discussed as follows. It has been reported that AHC is dominated by $\Omega(\mathbf{k})$ spikes at limited \mathbf{k} -points, where the spin-orbit-split bands cross the Fermi energy E_F [38, 39]. These spikes are caused by the small energy gaps between the n th and the m th bands (one occupied and one unoccupied), which lead to small energy denominators $[(\epsilon_{n\mathbf{k}} - \epsilon_{m\mathbf{k}})^2]$. Similar to AHC, the dominant contribution to *intra* SHC also comes from spikes in BZ. Moreover, at these \mathbf{k} -points, bands have analogous spin [37], indicating that around these $\tilde{\Omega}_\gamma(\mathbf{k})$ spikes, $\langle n\mathbf{k}|\hat{\sigma}_\gamma|n\mathbf{k}\rangle \approx \langle m\mathbf{k}|\hat{\sigma}_\gamma|m\mathbf{k}\rangle$, making Eq. (7) approximated as

$$\begin{aligned} \tilde{\Omega}_{n,\gamma}(\mathbf{k}) &\approx \langle n\mathbf{k}|\hat{\sigma}_\gamma|n\mathbf{k}\rangle \\ &\times \hbar^2 \sum_{m \neq n} \frac{-2 \text{Im}[\langle n\mathbf{k}|\hat{v}_x|m\mathbf{k}\rangle \langle m\mathbf{k}|\hat{v}_y|n\mathbf{k}\rangle]}{(\epsilon_{n\mathbf{k}} - \epsilon_{m\mathbf{k}})^2} \quad (10) \\ &= \langle n\mathbf{k}|\hat{\sigma}_\gamma|n\mathbf{k}\rangle \Omega_n(\mathbf{k}). \end{aligned}$$

Equation (10) illustrates that the spin of eigenstate is the bridge to connect Berry curvature and *intra* spin Berry curvature. On the other hand, only considering the direction, $\hat{\mathbf{m}} = \frac{\mathbf{m}}{|\mathbf{m}|}$ is used to denote the unit vector of magnetization. This unit vector is projected onto three

axes as $\hat{\mathbf{m}} = [m_x, m_y, m_z]$, and

$$m_\gamma \sim \int_{\text{BZ}} \frac{d^2k}{(2\pi)^2} \sum_n f_{n\mathbf{k}} \langle n\mathbf{k}|\hat{\sigma}_\gamma|n\mathbf{k}\rangle. \quad (11)$$

Considering Eqs. (3), (10), and (11), AHC and *intra* SHC can be related by the following formula

$$\boldsymbol{\sigma}_{\text{SH}}^{\text{intra}} \approx \eta \sigma_{\text{AH}} \hat{\mathbf{m}}, \quad (12)$$

where $\boldsymbol{\sigma}_{\text{SH}}^{\text{intra}} = [\sigma_{\text{SH},x}^{\text{intra}}, \sigma_{\text{SH},y}^{\text{intra}}, \sigma_{\text{SH},z}^{\text{intra}}]$, the coefficient η denotes the conversion efficiency from AHC to *intra* SHC. It should be mentioned that $\boldsymbol{\sigma}_{\text{SH}}^{\text{intra}}$, η , σ_{AH} depend on $\hat{\mathbf{m}}$, which is omitted in Eq. (12) for brevity. The approximation is due to that $\langle n\mathbf{k}|\hat{\sigma}_\gamma|n\mathbf{k}\rangle$ is not a good quantum number, and it will be shown that this approximation is negligible in the case of Eq. (12). More significantly, $\boldsymbol{\sigma}_{\text{SH}}^{\text{intra}}$ can be regarded as the intrinsic SAHE, since it denotes the spin current converted from AHE, and its spin orientation is along the magnetization. In a nutshell, the rigorous deviations of SAHE are presented using Kubo formula [Eqs. (7)-(9)], making AHE and SAHE correlated through the magnetization within the approximation $\langle n\mathbf{k}|\hat{\sigma}_\gamma|n\mathbf{k}\rangle \approx \langle m\mathbf{k}|\hat{\sigma}_\gamma|m\mathbf{k}\rangle$.

In the above section, the diagonal elements of spin matrix has been considered in order to define *intra* SHC. Meanwhile, the off-diagonal part also contributes to spin current. Through inserting $\sum_t |t\mathbf{k}\rangle \langle t\mathbf{k}| = 1$ into Eq. (6) and considering $t \neq n, m$, respectively, the off-diagonal part, called *inter* spin Berry curvature, is defined as

$$\begin{aligned} \tilde{\Omega}_{n,\gamma}(\mathbf{k}) = & \hbar^2 \sum_{\substack{m \neq n \\ t \neq m, n}} -\text{Im} \left[\langle n\mathbf{k}|\hat{\sigma}_\gamma|t\mathbf{k}\rangle \times \frac{\langle t\mathbf{k}|\hat{v}_x|m\mathbf{k}\rangle \langle m\mathbf{k}|\hat{v}_y|n\mathbf{k}\rangle}{(\epsilon_{n\mathbf{k}} - \epsilon_{m\mathbf{k}})^2} \right. \\ & \left. + \langle t\mathbf{k}|\hat{\sigma}_\gamma|m\mathbf{k}\rangle \times \frac{\langle n\mathbf{k}|\hat{v}_x|t\mathbf{k}\rangle \langle m\mathbf{k}|\hat{v}_y|n\mathbf{k}\rangle}{(\epsilon_{n\mathbf{k}} - \epsilon_{m\mathbf{k}})^2} \right]. \quad (13) \end{aligned}$$

With this quantity and its summation, *inter* spin Hall conductivity is defined as

$$\tilde{\Omega}_\gamma(\mathbf{k}) = \sum_n f_{n\mathbf{k}} \tilde{\Omega}_{n,\gamma}(\mathbf{k}), \quad (14)$$

$$\sigma_{\text{SH},\gamma}^{\text{inter}} = -\frac{e^2}{\hbar} \int_{\text{BZ}} \frac{d^2k}{(2\pi)^2} \tilde{\Omega}_\gamma(\mathbf{k}). \quad (15)$$

For the sake of intelligibility, all of the terminologies and symbols used above are summarized in Supplemental Material [37].

AHC and SHC.—The *ab initio* calculations have been performed to obtain AHC and SHC with rotating magnetization as depicted in Fig. 1(d), and the results at E_F are summarized in Fig. 2. Although it is conventional to set $\hat{\mathbf{m}}$ along z -axis to maximize AHC, indeed, AHC is dependent on $\hat{\mathbf{m}}$ [42]. Breaking the time-reversal symmetry (\mathcal{T}) [43], AHC shall be expressed by the odd-order terms

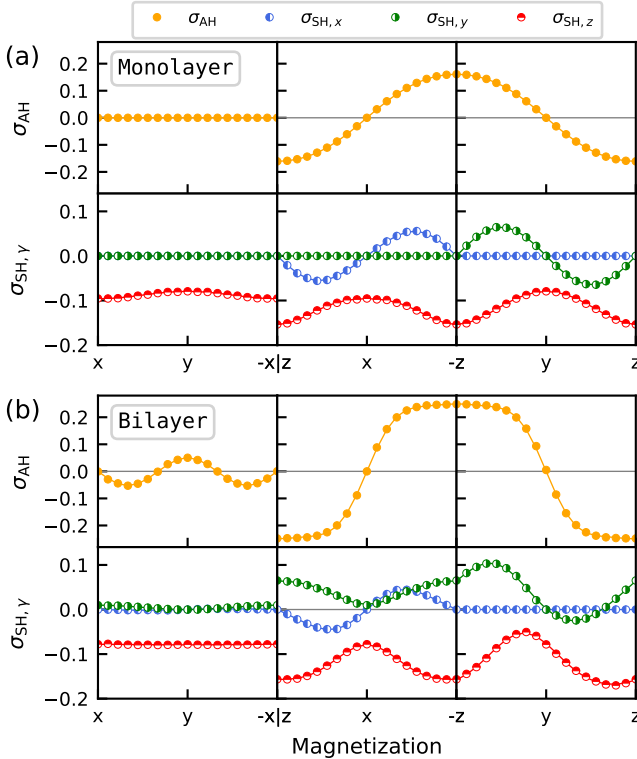


FIG. 2. AHC and SHC of (a) monolayer and (b) bilayer FGT with magnetization rotating inside xy -, xz -, and yz -planes. σ_{AH} of xy -magnetization is magnified 10 times in (b). Markers denote the *ab initio* data, while lines depict the fitting curves. SHC has been multiplied by a factor of $-2e/\hbar$, thus the units of both σ_{AH} and $\sigma_{\text{SH},\gamma}$ are e^2/\hbar .

with respect to magnetization. On the contrary, SHC is invariant under \mathcal{T} [43] and described by even-order terms. The fitting curves of the *ab initio* data are obtained using SciPy package [44], and the complete expressions can be found in Supplemental Material [37].

Figure 2(a) presents the AHC and SHC of monolayer FGT. It can be observed that $\sigma_{\text{AH}} = 0$ when the magnetization is in the xy -plane. In contrast, both the xz - and yz -magnetization cases allow the occurrence of AHC. When $\hat{\mathbf{m}}$ is along $-z$, the magnitude of AHC reaches the maximum, $0.134 e^2/h$, larger than other vdW ferromagnet [45]. According to the directions of spin polarization, σ_{SH} is decomposed into $\sigma_{\text{SH},x}$, $\sigma_{\text{SH},y}$, $\sigma_{\text{SH},z}$. Compared with the nonmagnetic transition metal dichalcogenides [46], the monolayer FGT can exhibit much larger SHC. Besides, the SHC in FGT is nonlinear and periodic with respect to $\hat{\mathbf{m}}$, indicating the magnitude of spin current can be controlled by magnetization. More intriguingly, various tensors emerge in FGT, making this system more practical for applications. For instance, when the magnetization is in the xz -plane, $\sigma_{\text{SH},x}$ and $\sigma_{\text{SH},z}$ tensors appear simultaneously, making the spin current induce both in-plane and out-of-plane torques.

Different from the monolayer, the bilayer FGT, with \mathcal{P} symmetry, can exhibit non-zero σ_{AH} with a period of $2\pi/3$ in the case of xy -magnetization [see Fig. 2(b)]. This can be explained by Neumann's principle, which states that the symmetry of physical property must include all the symmetries of crystal [30, 31, 47]. Since the magnetization is a pseudovector, when $\hat{\mathbf{m}}$ is orthogonal to any mirror shown in Fig. 1(c), \mathcal{M} would be preserved, thus prohibiting the occurrence of AHC. Consequently, $\sigma_{\text{AH}} = 0$ occurs periodically. When $\hat{\mathbf{m}}$ points to other orientations, mirrors would be broken and not restrict AHC. Besides, compared with the monolayer, a larger AHC of $0.248 e^2/h$ is found in the bilayer FGT. It is worth noting that more diverse SHC tensors are found in the bilayer FGT. In the xz -magnetization scenario, $\sigma_{\text{SH},x}$, $\sigma_{\text{SH},y}$, and $\sigma_{\text{SH},z}$ tensors can all occur simultaneously. The existence of $\sigma_{\text{SH},y}$ in bilayer FGT is distinct from that in monolayer FGT. The reason is attributed to the difference in symmetry, i.e., the xz -magnetization monolayer preserves the \mathcal{TC} (\mathcal{C} denotes the rotational symmetry) while the bilayer not, thus the latter can stimulate peculiar SHC tensor. The present findings evidently demonstrate that the interplay between magnetism and symmetry is effective to manipulate the magnitude and polarization of spin current.

Conversion from AHC to SAHC.—It has been discussed that SHC can be decomposed into *intra* SHC and *inter* SHC, and the *intra* SHC (i.e. SAHC) depends on AHC. The conversion from AHC to *intra* SHC is essential to comprehend *intra* SHC. Through *ab initio* calculations, the AHC and *intra* SHC with xz -magnetization have been investigated [see markers in Figs. 3(a) and (c)], note the *intra* SHC was calculated using the *intra* spin Berry curvature [Eqs. (7)-(9)]. Using Eq. 12, the conversion efficiency η from AHC to *intra* SHC can be derived by $\sigma_{\text{SH},\gamma}^{\text{intra}}/(m_\gamma\sigma_{\text{AH}})$, and η is displayed by

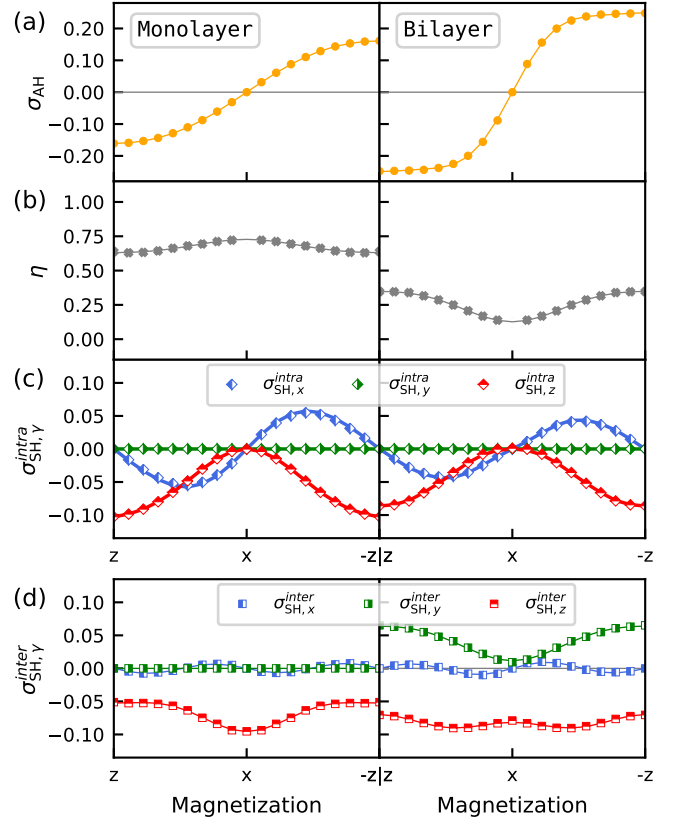


FIG. 3. (a) AHC, (b) conversion efficiency, (c) *intra* SHC, and (d) *inter* SHC of monolayer and bilayer FGT, respectively, with the xz -magnetization. The colorful markers in (a), (c), and (d) denote the *ab initio* data, while the grey markers in (b) are derived data. (a), (b), and (d) depict the fitting curves (slim lines), while (c) depicts the curves of Eq. (12) [see bold lines]. The units of σ_{AH} , $\sigma_{\text{SH},\gamma}^{\text{intra}}$, and $\sigma_{\text{SH},\gamma}^{\text{inter}}$ are e^2/h .

markers in Fig. 3(b). Using fitting functions of AHC and η , the evolution of *intra* SHC with respect to $\hat{\mathbf{m}}$ can be obtained using Eq. (12). Figure 3(c) illustrates that in both monolayer and bilayer FGT, the evolution curves of Eq. (12) [see bold lines] can perfectly characterize the *ab initio* data of *intra* SHC for any tensor element and any magnetization direction, demonstrating that the set of conversion efficiency is universal. Moreover, the case of yz -magnetization draws the same conclusion with the same η parameters [37]. Thus, the correlation between AHC and *intra* SHC, i.e. Eq. (12), is verified. Indeed, the anomalous Hall current is always accompanied by spin anomalous Hall current, with a spin orientation collinear with $\hat{\mathbf{m}}$ [14]. Consequently, *intra* SHC is expected to be dependent on AHC. The multiplier $\hat{\mathbf{m}} = [m_x, m_y, m_z]$ can be regarded as the projection onto x -, y -, and z -direction, producing three spin current components $\sigma_{\text{SH},x}^{\text{intra}}$, $\sigma_{\text{SH},y}^{\text{intra}}$, $\sigma_{\text{SH},z}^{\text{intra}}$, respectively.

Different from the *intra* SHC, there is no universal conversion efficiency from AHC to *inter* SHC, which is shown in the separated Fig. 3(d). It is worth mentioning that even if the spin orientates inside the xz -plane, *inter* SHC

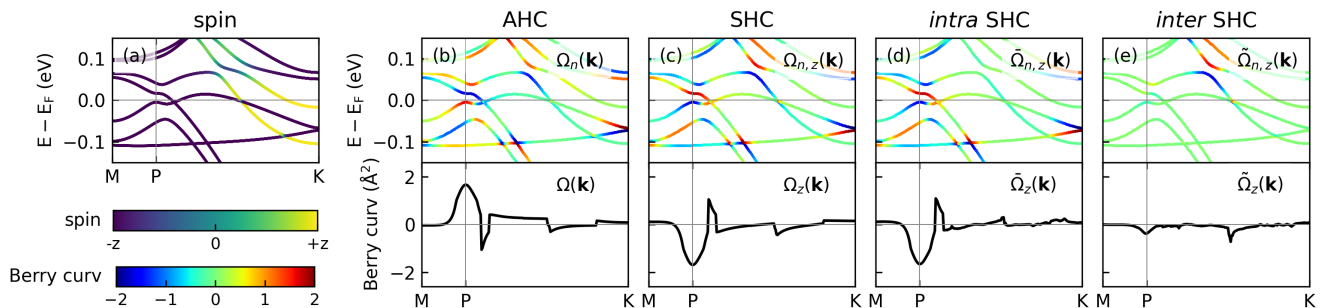


FIG. 4. (a) Spin projected bands of bilayer FGT with z -magnetization, the dark (bright) color denotes spin along $-z$ ($+z$). (b) Berry curvature, (c) spin Berry curvature, (d) *intra* spin Berry curvature, and (e) *inter* spin Berry curvature. The upper panels show the Berry curvatures projected bands, and the lower panels depict the summation results. All the Berry curvatures are in log scale [Eq. S9], the blue (red) color denotes the negative (positive) curvature value. The titles indicate the corresponding conductivities. E_F is set to zero.

can still contribute to the y -polarization (non-zero tensor $\sigma_{\text{SH},y}^{\text{inter}}$) in bilayer FGT, i.e., the y -polarization SHC is exclusively contributed by *inter* SHC.

Berry curvatures.—The band structures of bilayer FGT have been investigated to present the microscopic mechanism of the Hall conductivities. The Te- p and Fe- d orbitals make the dominant contributions to the bands around Fermi energy [37]. The projected bands along M-K are selected to clarify the correlations of various Berry curvatures. Figure 4(a) shows that at E_F , the spin orientations are well (anti-)aligned with the magnetization. Figures 4(b)-(e) present the *ab initio* results of various Berry curvatures. It can be seen that main contributions to Berry curvatures come from the band pairs with small energy gaps. As expected, for both $\Omega(\mathbf{k})$ and $\tilde{\Omega}_z(\mathbf{k})$, large spikes only occur at limited \mathbf{k} -points such as the P point, where the bands have analogous spin. On the contrary, $\tilde{\tilde{\Omega}}_z(\mathbf{k})$ is mainly contributed by the bands with misaligned spin away from E_F .

The conversion from AHC to *intra* SHC has been studied from the conductivity aspect in Fig. 3. To reveal the microscopic mechanisms, the conversion from Berry curvature to *intra* spin Berry curvature would be discussed at two levels: (i) The band-resolved conversion efficiency $\eta_n(\mathbf{k}) = \tilde{\tilde{\Omega}}_{n,z}(\mathbf{k})/\Omega_n(\mathbf{k})$, and (ii) the summation result $\eta(\mathbf{k}) = \tilde{\tilde{\Omega}}_z(\mathbf{k})/\Omega(\mathbf{k})$. Figures 4(a), (b), and (d) demonstrate that the $\eta_n(\mathbf{k})$ is determined by the spin of eigenstate, making $\eta_n(\mathbf{k}) = \langle n\mathbf{k}|\hat{\sigma}_z|n\mathbf{k}\rangle = \pm 1$ when the spin is collinear with the magnetization. For instance, two bands around E_F (one occupied and one unoccupied) at P point have spin along $-z$, i.e. $\eta_n(\mathbf{k}) = -1$, leading to the opposite signs of $\Omega_n(\mathbf{k})$ and $\tilde{\tilde{\Omega}}_{n,z}(\mathbf{k})$ on these two bands, as shown in the upper panels of Figs. 4(b) and (d). On the other hand, although $\Omega(\mathbf{k})$ [$\tilde{\tilde{\Omega}}_z(\mathbf{k})$] is a property of the occupied manifold, it is mostly determined by the band structure nearby Fermi surface, since the contributions of bands far away from E_F are cancelled by each other [48, 49]. Consequently, $\eta(\mathbf{k})$, to some extent, is determined by the spin of occupied state around E_F . For instance, at P point, the last occupied band exhibits spin along $-z$, resulting in $\eta(\mathbf{k}) = -1$ as shown in the lower

panels of Figs. 4(b) and (d). Note that the conductivities σ_{AH} and $\sigma_{\text{SH},z}^{\text{intra}}$ are, respectively, the integral of $\Omega(\mathbf{k})$ and $\tilde{\tilde{\Omega}}_z(\mathbf{k})$ with respect to \mathbf{k} . However, it should be emphasized that η is not the integral of $\eta(\mathbf{k})$ with respect to \mathbf{k} , since neither $\Omega(\mathbf{k})$, $\tilde{\tilde{\Omega}}_z(\mathbf{k})$ nor $\eta(\mathbf{k})$ is a constant in the Brillouin zone of FGT [37]. In fact, there is no simple relation between the global conversion efficiency η and the microscopic $\eta_n(\mathbf{k})$ in the FGT system. Thus, the global η shall be obtained using the global conductivities AHC and *intra* SHC, and the value of η is not restricted in the range of $[-1, 1]$.

Effective model.—An effective $k\cdot p$ model is constructed to reveal more physical principles. Under the basis of $[c_{1,k\uparrow}, c_{2,k\uparrow}, c_{1,k\downarrow}, c_{2,k\downarrow}]^T$ where 1 and 2 denote orbital index, the 4×4 Hamiltonian can be expressed as

$$H = (mk^2 + \delta)\tau_z + \alpha k_x \sigma_z \otimes \tau_x + \beta k_y \sigma_0 \otimes \tau_y + M \sigma_z \otimes \tau_0, \quad (16)$$

where σ_i and τ_i are Pauli matrices for the spin and orbital degrees of freedom, respectively. m denotes the effective mass, δ is the strength of band inversion. α and β terms respectively denote the SOC and the orbital hybridization. The last term indicates a magnetic field along z direction. This model qualitatively characterizes the *ab initio* bands around P point and E_F shown in Fig. 4, as well as the properties of spin and Berry curvatures. Moreover, it reveals that both Ω_n and $\tilde{\tilde{\Omega}}_{n,z}$ are proportional to the strength of the orbital hybridization while inversely proportional to SOC and band inversion [37].

Summary.—The origin and control of spin current in both monolayer and bilayer Fe_3GeTe_2 have been systematically investigated. It exhibits nonlinear behavior with respect to magnetization, as well as the simultaneous occurrence of in-plane and out-of-plane spin polarizations. Superior to the monolayer case, bilayer Fe_3GeTe_2 can present unusual arbitrary spin current tensor due to the reduced symmetry. Using the concepts of Berry curvatures and *intra* spin Berry curvature, the correlation between anomalous Hall effect and spin anomalous Hall effect has been clarified, as well as the corresponding con-

version efficiency. An effective $k \cdot p$ model illustrates that the orbital hybridization is essential for Berry curvatures. The present research demonstrates that the interplay between magnetism and symmetry can control both magnitude and polarization of the spin current, further stimulating exotic spin-orbit torques for spintronic devices.

Acknowledgments.—Jiaqi Zhou acknowledges fruitful discussions with Junfeng Qiao. The authors acknowledge financial support from the Fédération Wallonie-Bruxelles through the ARC entitled “3D nanoarchitec-

turing of 2D crystals” project (ARC 16/21-077), from the European Union’s Horizon 2020 research and innovation programme (Core3 - N° 881603), from the Flag-ERA JTC 2019 project entitled “SOGraPhMEM” (R.8012.19), and from the Belgium F.R.S-FNRS under the conventions N° T.0051.18. Computational resources have been provided by the supercomputing facilities of the Université catholique de Louvain (CISM) and the Consortium des Equipements de Calcul Intensif en Fédération Wallonie Bruxelles (CECI) funded by the Fonds de la Recherche Scientifique de Belgique (F.R.S-FNRS - N° 2.5020.11).

-
- [1] B. Dieny, I. L. Prejbeanu, K. Garello, P. Gambardella, P. Freitas, R. Lehdorff, W. Raberg, U. Ebels, S. O. Demokritov, J. Akerman, A. Deac, P. Pirro, C. Adelman, A. Anane, A. V. Chumak, A. Hirohata, S. Mangin, S. O. Valenzuela, M. C. Onbasli, M. D’Aquino, G. Prenat, G. Finocchio, L. Lopez-Diaz, R. Chantrell, O. Chubykalo-Fesenko, and P. Bortolotti, *Nat. Electron.* **3**, 446 (2020).
- [2] S. Peng, D. Zhu, J. Zhou, B. Zhang, A. Cao, M. Wang, W. Cai, K. Cao, and W. Zhao, *Adv. Electron. Mater.* **5**, 1900134 (2019).
- [3] S. Ikeda, K. Miura, H. Yamamoto, K. Mizunuma, H. D. Gan, M. Endo, S. Kanai, J. Hayakawa, F. Matsukura, and H. Ohno, *Nat. Mater.* **9**, 721 (2010).
- [4] R. Ramaswamy, J. M. Lee, K. Cai, and H. Yang, *Appl. Phys. Rev.* **5**, 031107 (2018).
- [5] A. Manchon, J. Železný, I. M. Miron, T. Jungwirth, J. Sinova, A. Thiaville, K. Garello, and P. Gambardella, *Rev. Mod. Phys.* **91**, 035004 (2019).
- [6] L. Liu, O. J. Lee, T. J. Gudmundsen, D. C. Ralph, and R. A. Buhrman, *Phys. Rev. Lett.* **109**, 096602 (2012).
- [7] L. Zhu, D. C. Ralph, and R. A. Buhrman, *Phys. Rev. Lett.* **122**, 077201 (2019).
- [8] J. Sinova, S. O. Valenzuela, J. Wunderlich, C. H. Back, and T. Jungwirth, *Rev. Mod. Phys.* **87**, 1213 (2015).
- [9] M. Wang, W. Cai, D. Zhu, Z. Wang, J. Kan, Z. Zhao, K. Cao, Z. Wang, Y. Zhang, T. Zhang, C. Park, J.-P. Wang, A. Fert, and W. Zhao, *Nat. Electron.* **1**, 582 (2018).
- [10] G. Yu, P. Upadhyaya, Y. Fan, J. G. Alzate, W. Jiang, K. L. Wong, S. Takei, S. A. Bender, L.-T. Chang, Y. Jiang, M. Lang, J. Tang, Y. Wang, Y. Tserkovnyak, P. K. Amiri, and K. L. Wang, *Nat. Nanotechnol.* **9**, 548 (2014).
- [11] L. Liu, C. Zhou, X. Shu, C. Li, T. Zhao, W. Lin, J. Deng, Q. Xie, S. Chen, J. Zhou, R. Guo, H. Wang, J. Yu, S. Shi, P. Yang, S. Pennycook, A. Manchon, and J. Chen, *Nat. Nanotechnol.* **16**, 277 (2021).
- [12] D. MacNeill, G. M. Stiehl, M. H. D. Guimaraes, R. A. Buhrman, J. Park, and D. C. Ralph, *Nat. Phys.* **13**, 300 (2017).
- [13] J. H. Garcia, M. Vila, C.-H. Hsu, X. Waintal, V. M. Pereira, and S. Roche, *Phys. Rev. Lett.* **125**, 256603 (2020).
- [14] T. Taniguchi, J. Grollier, and M. D. Stiles, *Phys. Rev. Applied* **3**, 044001 (2015).
- [15] Y. Koike, S. Iihama, and S. Mizukami, *Jpn. J. Appl. Phys.* **59**, 090907 (2020).
- [16] S. Varotto, M. Cosset-Chéneau, C. Grèzes, Y. Fu, P. Warin, A. Brenac, J.F. Jacquot, S. Gambarelli, C. Rinaldi, V. Baltz, J.-P. Attané, L. Vila, and P. Noël, *Phys. Rev. Lett.* **125**, 267204 (2020).
- [17] J. Cramer, A. Ross, S. Jaiswal, L. Baldrati, R. Lebrun, and M. Kläui, *Phys. Rev. B* **99**, 104414 (2019).
- [18] N. Nagaosa, J. Sinova, S. Onoda, A. H. MacDonald, and N. P. Ong, *Rev. Mod. Phys.* **82**, 1539 (2010).
- [19] Y. Omori, E. Sagasta, Y. Niimi, M. Gradhand, L. E. Hueso, F. Casanova, and Y. C. Otani, *Phys. Rev. B* **99**, 014403 (2019).
- [20] S. Iihama, T. Taniguchi, K. Yakushiji, A. Fukushima, Y. Shiota, S. Tsunegi, R. Hiramatsu, S. Yuasa, Y. Suzuki, and H. Kubota, *Nat. Electron.* **1**, 120 (2018).
- [21] T. Seki, S. Iihama, T. Taniguchi, and K. Takanashi, *Phys. Rev. B* **100**, 144427 (2019).
- [22] T. C. Chuang, D. Qu, S. Y. Huang, and S. F. Lee, *Phys. Rev. Research* **2**, 032053(R) (2020).
- [23] V. P. Amin, J. Li, M. D. Stiles, and P. M. Haney, *Phys. Rev. B* **99**, 220405(R) (2019).
- [24] A. Davidson, V. P. Amin, W. S. Aljuaid, P. M. Haney, and X. Fan, *Phys. Lett. A* **384**, 126228 (2020).
- [25] G. Qu, K. Nakamura, and M. Hayashi, *Phys. Rev. B* **102**, 144440 (2020).
- [26] K. S. Burch, D. Mandrus, and J.-G. Park, *Nature* **563**, 47 (2018).
- [27] X. Lin, W. Yang, K. L. Wang, and W. Zhao, *Nat. Electron.* **2**, 274 (2019).
- [28] Z. Fei, B. Huang, P. Malinowski, W. Wang, T. Song, J. Sanchez, W. Yao, D. Xiao, X. Zhu, A. F. May, W. Wu, D. H. Cobden, J.-H. Chu, and X. Xu, *Nat. Mater.* **17**, 778 (2018).
- [29] Y. Deng, Y. Yu, Y. Song, J. Zhang, N. Z. Wang, Z. Sun, Y. Yi, Y. Z. Wu, S. Wu, J. Zhu, J. Wang, X. H. Chen, and Y. Zhang, *Nature* **563**, 94 (2018).
- [30] R. E. Newnham, *Properties of Materials: Anisotropy, Symmetry, Structure* (Oxford University Press, Oxford, England, UK, 2005).
- [31] S. V. Gallego, J. Etxebarria, L. Elcoro, E. S. Tasci, and J. M. Perez-Mato, *Acta Crystallogr., Sect. A* **75**, 438 (2019).
- [32] M. Seemann, D. Ködderitzsch, S. Wimmer, and H. Ebert, *Phys. Rev. B* **92**, 155138 (2015).
- [33] F. Freimuth, S. Blügel, and Y. Mokrousov, arXiv (2021), 2103.15663.
- [34] F. Freimuth, S. Blügel, and Y. Mokrousov, *Phys. Rev. Lett.* **105**, 246602 (2010).
- [35] P. Giannozzi, O. Andreussi, T. Brumme, O. Bunau, M. B. Nardelli, M. Calandra, R. Car, C. Cavazzoni, D. Ceresoli, M. Cococcioni, N. Colonna, I. Carnimeo,

- A. D. Corso, S. de Gironcoli, P. Delugas, R. A. DiStasio, A. Ferretti, A. Floris, G. Fratesi, G. Fugallo, R. Gebauer, U. Gerstmann, F. Giustino, T. Gorni, J. Jia, M. Kawamura, H.-Y. Ko, A. Kokalj, E. Küçükbenli, M. Lazzeri, M. Marsili, N. Marzari, F. Mauri, N. L. Nguyen, H.-V. Nguyen, A. O. de-la Roza, L. Paulatto, S. Poncé, D. Rocca, R. Sabatini, B. Santra, M. Schlipf, A. P. Seitsonen, A. Smogunov, I. Timrov, T. Thonhauser, P. Umari, N. Vast, X. Wu, and S. Baroni, *J. Phys.: Condens. Matter* **29**, 465901 (2017).
- [36] G. Pizzi, V. Vitale, R. Arita, S. Blügel, F. Freimuth, G. Géranton, M. Gibertini, D. Gresch, C. Johnson, T. Koretsune, J. Ibañez-Azpiroz, H. Lee, J.-M. Lihm, D. Marchand, A. Marrazzo, Y. Mokrousov, J. I. Mustafa, Y. Nohara, Y. Nomura, L. Paulatto, S. Poncé, T. Ponweiser, J. Qiao, F. Thöle, S. S. Tsirkin, M. Wierzbowska, N. Marzari, D. Vanderbilt, I. Souza, A. A. Mostofi, and J. R. Yates, *J. Phys.: Condens. Matter* **32**, 165902 (2020).
- [37] Supplemental Material.
- [38] Y. Yao, L. Kleinman, A. H. MacDonald, J. Sinova, T. Jungwirth, D.-s. Wang, E. Wang, and Q. Niu, *Phys. Rev. Lett.* **92**, 037204 (2004).
- [39] X. Wang, J. R. Yates, I. Souza, and D. Vanderbilt, *Phys. Rev. B* **74**, 195118 (2006).
- [40] J. Qiao, J. Zhou, Z. Yuan, and W. Zhao, *Phys. Rev. B* **98**, 214402 (2018).
- [41] J. Zhou, J. Qiao, A. Bournel, and W. Zhao, *Phys. Rev. B* **99**, 060408(R) (2019).
- [42] E. Roman, Y. Mokrousov, and I. Souza, *Phys. Rev. Lett.* **103**, 097203 (2009).
- [43] R. R. Birss, *Symmetry and Magnetism* (North-Holland Publishing Company, 1964).
- [44] SciPy, <https://www.scipy.org/>.
- [45] X. Yang, X. Zhou, W. Feng, and Y. Yao, *Phys. Rev. B* **103**, 024436 (2021).
- [46] W. Feng, Y. Yao, W. Zhu, J. Zhou, W. Yao, and D. Xiao, *Phys. Rev. B* **86**, 165108 (2012).
- [47] X. Zhou, J.-P. Hanke, W. Feng, F. Li, G.-Y. Guo, Y. Yao, S. Blügel, and Y. Mokrousov, *Phys. Rev. B* **99**, 104428 (2019).
- [48] X. Wang, D. Vanderbilt, J. R. Yates, and I. Souza, *Phys. Rev. B* **76**, 195109 (2007).
- [49] G. Y. Guo, S. Murakami, T.-W. Chen, and N. Nagaosa, *Phys. Rev. Lett.* **100**, 096401 (2008).